


ORIGINAL ARTICLE

Open Access



Understanding ADC variation by fat content effect using a dual-function MRI phantom

Yi-Jui Liu^{1†}, Tung-Sheng Tsai², Ya-Hui Li^{3†}, Jo-Hua Peng⁴, Hing-Chiu Chang⁵, Hsu-Hsia Peng⁴, Ying-Chieh Lee¹, Tung-Yang Lee^{6,7}, Chang-Hsien Liou^{3,8}, Tz-Feng Lin⁹, Fatt-Yang Chew^{10,11}, Ruey-Hwang Chou^{12,13,14*†}  and Chun-Jung Juan^{3,4,11*†}

Abstract

Background A dual-function phantom designed to quantify the apparent diffusion coefficient (ADC) in different fat contents (FCs) and glass bead densities (GBDs) to simulate the human tissues has not been documented yet. We propose a dual-function phantom to quantify the FC and to measure the ADC at different FCs and different GBDs.

Methods A fat-containing diffusion phantom comprised by 30 glass-bead-containing fat-water emulsions consisting of six different FCs (0, 10, 20, 30, 40, and 50%) multiplied by five different GBDs (0, 0.1, 0.25, 0.5, and 1.0 g/50 mL). The FC and ADC were measured by the “iterative decomposition of water and fat with echo asymmetry and least squares estimation-IQ”, IDEAL-IQ, and single-shot echo-planar diffusion-weighted imaging, SS-EP-DWI, sequences, respectively. Linear regression analysis was used to evaluate the relationship among the fat fraction (FF) measured by IDEAL-IQ, GBD, and ADC.

Results The ADC was significantly, negatively, and linearly associated with the FF (the linear slope ranged from -0.005 to -0.017, $R^2 = 0.925$ to 0.986 , all $p < 0.001$). The slope of the linear relationship between the ADC and the FF, however, varied among different GBDs (the higher the GBD, the lower the slope). ADCs among emulsions across different GBDs and FFs were overlapped. Emulsions with low GBDs plus high FFs shared a same lower ADC range with those with median or high GBDs plus median or lower FFs.

Conclusions A novel dual-function phantom simulating the human tissues allowed to quantify the influence of FC and GBD on ADC.

Relevance statement The study developed an innovative dual-function MRI phantom to explore the impact of FC on ADC variation that can affect clinical results. The results revealed the superimposed effect on FF and GBD density on ADC measurements.

Key points

- A dual-function phantom made of glass bead density (GBD) and fat fraction (FF) emulsion has been developed.
- Apparent diffusion coefficient (ADC) values are determined by GBD and FF.
- The dual-function phantom showed the mutual ADC addition between FF and GBD.

[†]Chun-Jung Juan, Ruey-Hwang Chou, Yi-Jui Liu, and Ya-Hui Li contributed equally to this work.

*Correspondence:

Ruey-Hwang Chou

rhchou@mail.cmu.edu.tw

Chun-Jung Juan

peterjuancj@yahoo.com.tw

Full list of author information is available at the end of the article

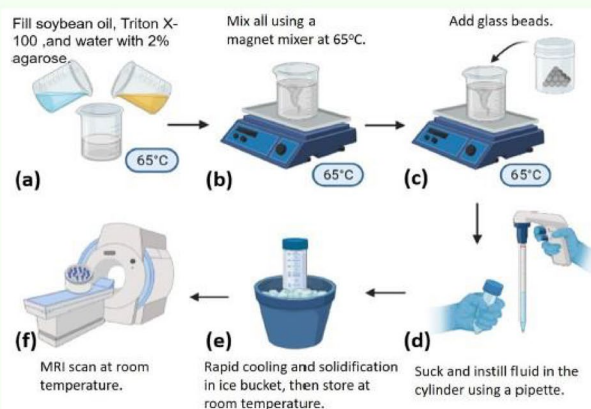
Keywords Adipose tissue, Diffusion magnetic resonance imaging, Phantoms (imaging), Quality assurance (healthcare), Quality control

Graphical Abstract

Understanding ADC variation by fat content effect using a dual-function MRI phantom

ESR[®] EUROPEAN SOCIETY OF RADIOLOGY

- A dual-function phantom made of glass bead density (GBD) and fat fraction (FF) emulsion has been developed.
- Apparent diffusion coefficient (ADC) values are determined by GBD and FF.
- The dual-function phantom showed the mutual ADC addition between FF and GBD.



The study developed an innovative dual-function MRI phantom to explore the impact of FC on ADC variation that can affect clinical results. The results revealed the superimposed effect on FF and GBD density on ADC measurements.

**Eur Radiol Exp (2024) Liu YJ, Tsai TS, Li YH et al;
DOI: 10.1186/s41747-023-00414-0**

European
Radiology
EXPERIMENTAL

Background

Magnetic resonance imaging (MRI) has been recognized to provide quantitative imaging biomarkers [1] by measuring tissue characteristics and function, including but not limited to brain volume [2], tumor volume [3], functional network connectivity [4], fat content (FC) [5], and diffusivity of tissue water [6]. Diffusion-weighted imaging (DWI) allows measuring proton diffusivity by calculating the apparent diffusion coefficient (ADC) [6], while the “iterative decomposition of water and fat with echo asymmetry and least squares estimation-IQ” (IDEAL-IQ) sequence allows measuring the FC of tissue [7].

In order to increase the reliability and comparability of data gathered from MRI biomarkers, standardization of imaging protocols and calibration of measures using phantoms are necessary to validate the accuracy of these measures *in vivo* [8]. Therefore, the Radiological Society of North America established the Quantitative Imaging Biomarkers Alliance and quantitative imaging protocols, phantoms, and technical standards documents [9]. There are many kinds of phantoms that provide different

functions. For example, the traditionally used American College of Radiology phantom is a system phantom allowing evaluation of the image quality and comparison across geometric distortion, slice positioning, thickness accuracy, high-contrast spatial resolution, intensity uniformity, ghosting artifact, and low-contrast object detectability [10]. Other phantoms include but not limited to diffusion phantom, which is designed for quantifying the ADC measurement [11], and water-fat phantom, which is used for monitoring and calibrating fat fraction measurement [12, 13].

Recently, various ADC phantoms made from tissue-equivalent materials have been developed to simulate the different forms of restricted Brownian motion of water. These phantoms serve multiple purposes, including optimizing DWI protocols and evaluating the accuracy and reproducibility of ADC measurements. Materials used in ADC phantoms can include varying concentrations of high-viscosity gelatinous substances to simulate different degrees of restricted Brownian motion of water, such as polyvinylpyrrolidone [14], polyethylene glycol [15, 16], polyacrylamide [17, 18], sucrose [19–21], and agarose

[17, 19]. Another approach involves using various densities of microparticles to mimic cell-occupied spaces and increase barrier concentration, resulting in different levels of restricted Brownian motion of water [11, 22].

However, a single-function phantom is not sufficient to fit real-world situations. For example, DWI might be performed in fat-containing tissue such as breast [23], salivary gland [24], and vertebra and measurement of the ADC value might be influenced by the content of fat in the breast. Taking breast lesion for example, a high ADC is interpreted as a sign of benign nature of the lesion, while a low ADC is classified as a sign of malignancy [25]. Subsequently, a fatty mass, such as fat necrosis, might be mistakenly interpreted as a malignancy due to its low ADC if the FC is not taken into account [25]. To avoid mistakenly interpreting a fat-containing mass with low ADC as a malignant lesion, simultaneous measures of both ADC and FC is crucial rather than single measure of ADC.

To the best of knowledge, a dual-function phantom designed to quantify the ADC in different FCs and different glass bead densities (GBDs) to simulate the human tissue has not been documented yet. In this study, we designed a novel dual-function phantom to allow us to quantify the FC and to measure the ADC at different FCs and different GBDs.

Methods

Phantom design

The composition of each cylindrical cone of a fat-containing diffusion phantom, which consisted of six different FCs (0, 10, 20, 30, 40, and 50%) *versus* five different GBDs (0, 0.1, 0.25, 0.5, and 1.0 g/50 mL), used in this study is shown in Table 1. In this phantom, various percentages of water and soybean oil emulsified by an emulsifying agent (Triton X-100) [26] were mixed with various GBDs (#K37, 3M microspheres, Easy Composites Ltd., Stoke, UK) [11]. Agarose was added into the emulsion to serve as a coagulating agent to prevent dissociation of the water-oil emulsion on the one hand and sinking/suspension of glass particles on the other hand [11].

The pipeline demonstrating the processes for preparing the proposed phantom is shown in Fig. 1. First of all, soybean oil and water at a certain ratio were mixed together with a nonionic surfactant (Triton X-100, Sigma-Aldrich, Massachusetts, USA) and a coagulant (2% agarose) at 65 °C (Fig. 1a). Second, fluid was stirred at a speed of 700 revolution per minute (RPM) for 2 min and then at a speed of 1,150 RPM for 5 min at 65 °C (Fig. 1b). Third, glass beads at a certain density were added with the fluid continuously stirred at a speed of 1,150 RPM for 2 min at 65 °C (Fig. 1c). Fourth, the mixture was sucked out and gradually instilled into a cylindrical cone (50 mL) using a pipette (Fig. 1d). Fifth, the cylindrical cone was put in the ice bucket to cool down rapidly. The sticky fluid turned to jelly immediately to keep the homogeneity of all components (Fig. 1e). Sixth, a phantom comprised by 30 glass-bead-containing fat-water emulsions consisting of six FFs multiplied by five GBDs was produced and put into a plastic container for MRI scans (Fig. 1f). Finally, a total of three repetitions, each containing 30 cylindrical cones, were prepared, respectively. The phantoms were stored in the MRI scan room for 1 day to allow their temperature to equilibrate with that of the MRI room. The MRI scan room temperature was maintained at a stable 20°C by the air conditioning system, with temperature monitoring conducted via the operation console of MRI vendor.

MRI protocols

All images were acquired using a 1.5-T scanner (Signa MR450, General Electric Healthcare, Chicago, USA). IDEAL-IQ sequence was applied to quantify the FC of the phantom [8]. The IDEAL method [27] was a three-dimensional fast spoiled gradient-echo sequence employing a six-echo acquisition (1.1 to 6.38 ms) with imaging parameters including repetition time of 19.6 ms, field of view of 220 × 220 mm, matrix size of 128 × 128, bandwidth of 90.91 kHz, flip angle of 5°, number of excitations 4, and slice thickness of 10 mm. DWI was performed using a single-shot echo-planar imaging (SS-EPI) sequence with water excitation and the scanning

Table 1 Composition of the proposed fat-containing diffusion phantom

FC (%)	Soybean oil (V%)	Triton X-100 (V%)	Water (V%)	GBD (g/50 mL)				
0	0.0	0.0	100					
10	10.0	0.4	89.6					
20	19.8	0.8	79.4	0.00	0.10	0.25	0.50	1.00
30	29.6	1.2	69.2					
40	39.4	1.6	59.0					
50	49.0	2.0	49.0					

FC Fat content (%), GBD Glass bead density (g/50 mL), V% Volume percentage

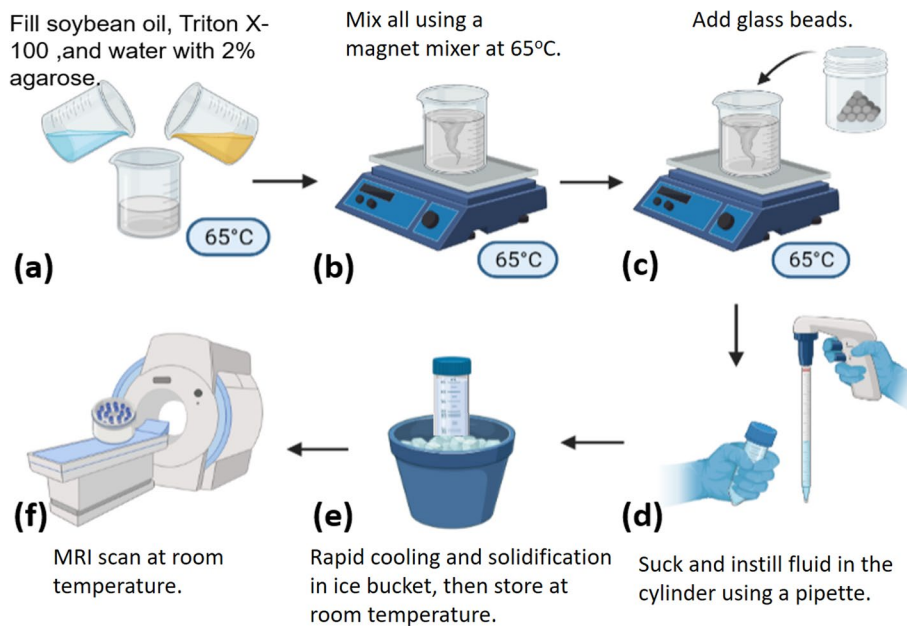


Fig. 1 The pipeline illustrating the processes for producing a fat-containing diffusion phantom. Soybean oil (yellow) and water (blue) were mixed together with a nonionic surfactant (Triton X-100) and a coagulant (2% agarose) at 65 °C (a). Fluid was stirred at a speed of 700 revolution per min (RPM) for 2 min and then at a speed of 1,150 RPM for 5 min at 65 °C (b). Glass beads were added with the fluid continuously stirred at a speed of 1,150 RPM for 2 min at 65 °C (c). The mixture was sucked out and gradually instilled into a cylindrical cone (50 mL) using a pipette (d). The cylindrical cone was put in the ice bucket to cool down rapidly to turn the sticky fluid into jelly to keep the homogeneity of all components (e). A phantom comprised by 30 glass-bead-containing fat-water emulsions consisting of six fat fractions multiplied by five glass bead densities was produced and put into a plastic container (f)

parameters including repetition time of 4,000 ms, echo time (TE) of 78.1 ms, b -values of 0 and 1,000 s/mm², 6 NEXs, FOV of 210 × 210 mm, slice thickness of 10 mm, matrix size of 128 × 128, and bandwidth of 250 kHz. The protocol parameters in IDEAL-IQ and DWI are summarized in Table 2.

Table 2 The protocol parameters for IDEAL-IQ and DWI sequences

	IDEAL-IQ	DWI
TR	19.6 ms	4,000 ms
TE	6 echoes (1.12, 3.008, 4.896, 6.784, 8.672, and 10.56 ms)	78.1 ms
NEX	4	4 ($b = 0$), 6 ($b = 1,000$ s/mm ²)
FOV	220 × 220 mm	210 × 210 mm
Matrix size	128 × 128	128 × 128
Slice Thickness	10 mm	10 mm
FA	5°	90°
Bandwidth	90.91 kHz	250.00 kHz
Acquisition time	1 min 38 s	1 min 32 s

FA Flip angle, FOV Field of view, NEX Number of excitations, TE Echo time, TR Repetition time. See the text for the denomination of the sequences

Imaging processing

Proton-density fat fraction maps were automatically generated by the MRI scanner. ADC maps were generated via pixel-by-pixel computation from b_0 and b_{1000} images basing on the Stejskal–Tanner relationship: $ADC = \ln(S_{b=0}/S_{b=1000})/b$. In both DWI and IDEAL-IQ scan, an axial slice, which was perpendicular to the long axis of cylindrical cones and contained the largest cross-sectional area of the phantom, was chosen for region-of-interest selection. Circular region-of-interests with one in each cylindrical cone were placed avoiding the partial volume effect of the cylindrical wall and extra-cylindrical noise. A total of three repetitions, each comprising 30 combos with five GBDs (0, 0.1, 0.25, 0.5, and 1.0 g/50 mL) and six FCs (0, 10, 20, 30, 40, and 50%) (Table 1), were prepared in order to evaluate test-retest reliability among different measures. Thus, each combo of the phantom was measured three times independently.

Statistical analysis

All values were presented as mean and standard deviations. Linear regression analysis was used to evaluate the relationship among the FF, GBD, and ADC values. Intraclass correlation coefficient and coefficient of variation were used to evaluate test-retest reliability among

measures of 3 different phantoms. A *p* value less than 0.05 was considered statistically significant.

Results

The coefficient of variation was 4.1 and 1.8% for in measuring ADC and FF, respectively. The intraclass correlation coefficient was 0.997 and 0.999 for in measuring ADC and FF, respectively, for three different phantoms, suggestive of excellent reliability as suggested by Koo et al. [28].

The gross and microscopic appearances of the proposed phantom are partly demonstrated in Fig. 2. Figure 2a demonstrates 5 cylindrical cones, which contained agarose-based fat-water emulsions with FC of 10, 20, 30, 40, and 50%, respectively. These cylindrical cones were intentionally placed horizontally in order to demonstrate the solidity of these fat-water emulsions at the room temperature. Figure 2b demonstrates six microscopic images mixing GBDs (0, 0.1g/50 mL, and 0.5g/50 mL) and fat-water emulsions (FC 10 and 30%), showing the geometric distribution and arrangement of glass beads, fat droplets, and water in the emulsion.

The imaging appearance and performance in estimating the FC using the IDEAL-IQ under different GBDs were demonstrated in Fig. 3. Figure 3a illustrates the PDFF maps of emulsions with the FF varying from 10 to 50% and the GBD ranging from 0 to 0.5 g/50 mL. Figure 3b demonstrates scatter plots of the FF measured by the IDEAL-IQ and the FC in the originally prepared phantom, showing significantly linear relationship between the FF and the FC ($y = ax + b$ with slope *a* ranging from

1.026 to 1.051, bias *b* ranging from -0.191 to 0.8, R^2 ranging from 0.998 to 0.999, and all $p < 0.001$) in all GBDs. One slice of DWI and ADC using SS-EP-DWI sequence is shown in Fig. 4. The imaging appearance and performance of the phantom in measuring the ADC value using SS-EP-DWI under different FFs are shown in Fig. 5. Figure 5a shows the cropped DWI ($b = 0$ and 1000 s/mm^2 , respectively) and ADC maps under the FF of 10, 30, and 50%. Figure 5b displays a significant and inverse linear relationship ($y = -0.015x + 1.603$, $R^2 = 0.975$, $p < 0.001$) between the ADC and the FF without adding any glass beads (GBD = 0).

The imaging appearance and performance of the phantom in measuring the ADC value using SS-EP-DWI under different GBDs are shown in Fig. 6. Figure 6a shows the cropped DWIs ($b = 0$ and $1,000 \text{ s/mm}^2$, respectively) and the ADC maps with the GBD of 0, 0.25, and 0.5 g/50 mL, respectively. Figure 6b displays a significant and inverse linear relationship ($y = -0.12x + 1.563$, $R^2 = 0.982$, $p < 0.001$) between ADC and GBD without FC (= 0). The imaging appearance and performance of the phantom in measuring the ADC value using SS-EP-DWI under different FFs and GBDs are shown in Fig. 7. Figure 7a shows the cropped DWIs ($b = 0$ and $1,000 \text{ s/mm}^2$) and the ADC maps of the emulsions with FF of 10, 30, and 50%, at the GBD of 0.5 g/50 mL. Figure 7b displays the ADC versus FF scatter plots of the emulsions under the GBD of 0, 0.1 g/50 mL, 0.25 g/50 mL, 0.5 g/50 mL, and 1.0 g/50 mL, showing a significant and inverse linear relationship between the ADC and the FF at each GBD ($y = ax + b$, with *a* ranging from -0.005 to -0.017 and *b* ranging from

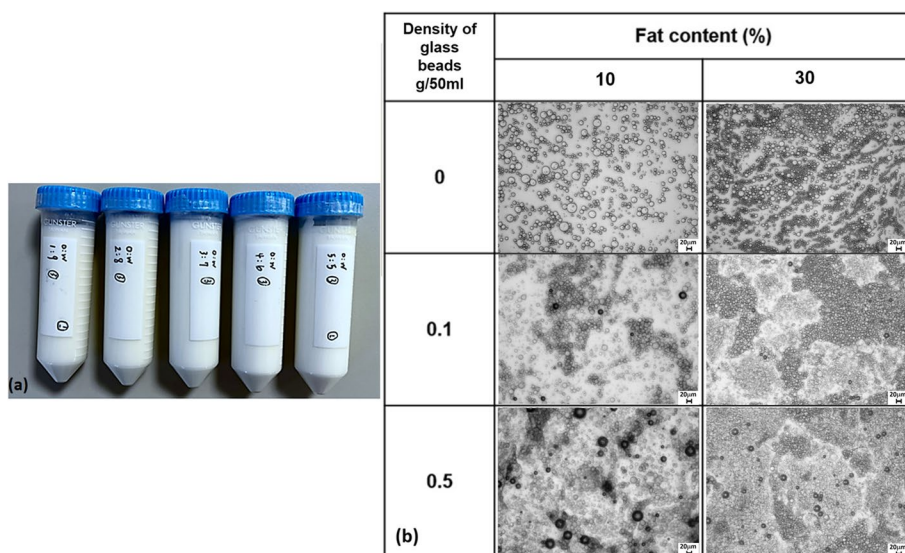


Fig. 2 a The fat-water phantom housing five cylinders containing agarose-based emulsions with a fat content of 10, 20, 30, 40, and 50% (left to right), respectively, was constructed. Vials are lying horizontally to demonstrate the solid nature of the phantom at room temperature. b Micrographs (x40) of 10% of fat content and 30% of fat content with 0, 0.1, and 0.5 g/50 mL of glass bead density, respectively

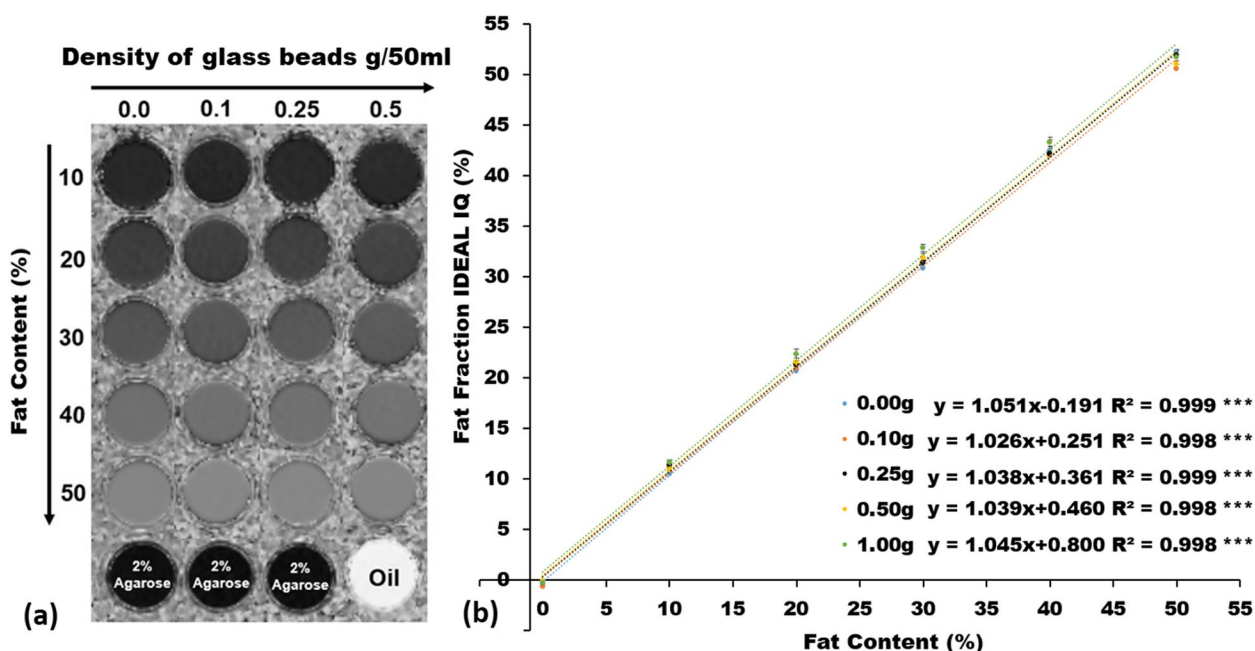


Fig. 3 **a** Fat fraction (FF) maps of IDEAL-IQ in 10, 20, 30, 40, and 50% of fat content (top to down) with respect to 0, 0.1, 0.25, and 0.5 g/50 mL of GBD (left to right). **b** Linear relationship between the FF measured by IDEAL-IQ and the fat content of phantom in different GBD of 0, 0.1, 0.25, 0.5, and 1.0 g/50 mL, respectively. *** $p < 0.001$

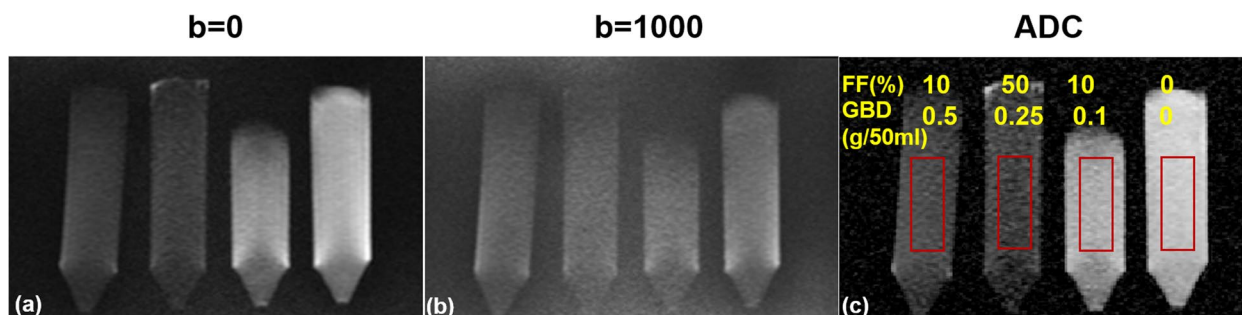


Fig. 4 One slice of the diffusion-weighted images: $b = 0$ s/mm² (a), $b = 1,000$ s/mm² (b), and the ADC map (c). The red rectangle indicates the location of the regions of interest. ADC Apparent diffusion coefficient

0.381 to 1.603, $R^2 = 0.925$ to 0.986, all $p < 0.001$), with a decreasing interception as the GBD increases. Figure 7c illustrates the overlapping phenomenon of ADC among emulsions across different GBDs and FFs. For example, emulsions with 0.1 g/50 mL GBDs plus 40–50% FFs shared a same lower ADC range with those with 0.5 g/50 mL GBDs plus 10~20% FFs. Likewise, emulsions with zero GBDs but 50% FFs had a median ADC range overlapped by those with 0.1 g/50 mL GBDs plus 30% FFs and those with 0.25 g/50 mL GBDs plus 20% FFs.

Table 3 shows all ADC values (mean \pm standard deviation) of all 30 emulsions within five GBDs (0, 0.1, 0.25, 0.5, and 1.0 g/50 mL) and six FFs (0, 10, 20, 30, 40, and 50%).

Discussion

Currently, fat-water phantoms and diffusion phantoms have been used to validate MRI-based methods in quantifying the FC [12, 29–33] and to measure the diffusivity of polyethylene particle suspensions or microbead impregnated gels on DWI [11, 19, 34, 35], respectively. However, these phantoms do not enable us to clarify the impact of FC on the measure of the diffusivity of polyethylene or microbead preparations in any single phantom. Under this circumstance, it remains controversial regarding the role of fat on measuring the diffusivity of a phantom. In humans, the FC measured by the IDEAL method [36] varies across age, gender, and body mass index in parotid glands [24] and spine [37–39], and has a

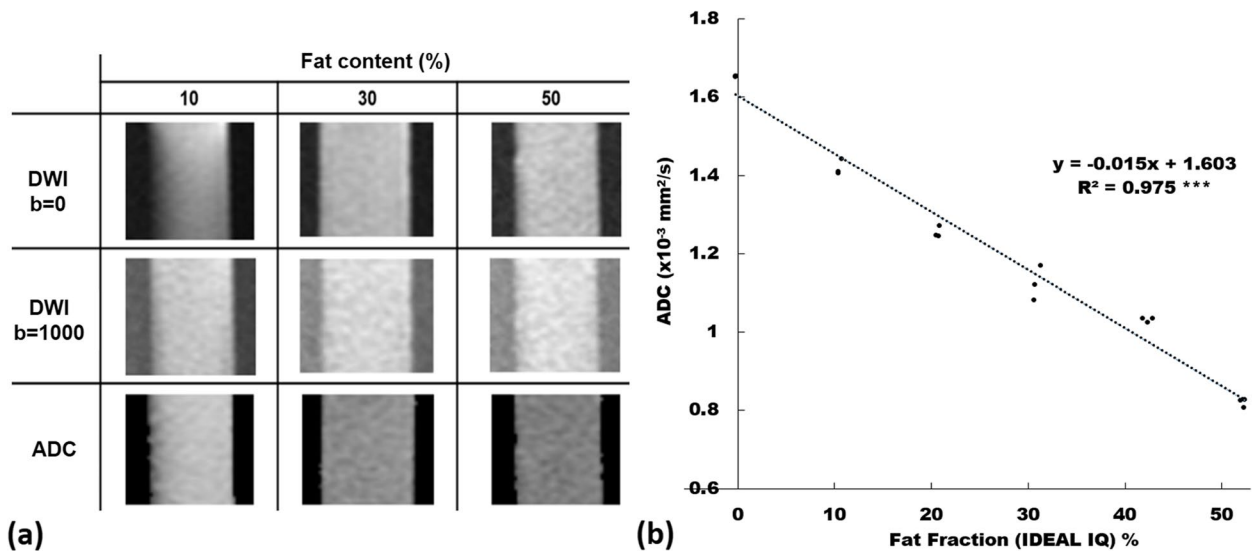


Fig. 5 **a** Diffusion-weighted images ($b = 0$ s/mm² and $b = 1,000$ s/mm²) and ADC maps of emulsions comprising fat content of 10, 30, and 50% plus 2% agarose and water without adding any glass beads. **b** Scatter plot and linear regression (dotted line) of ADC versus fat fraction measured by IDEAL-IQ (see the text for this sequence) among three independently prepared phantoms. ADC Apparent diffusion coefficient. *** $p < 0.001$

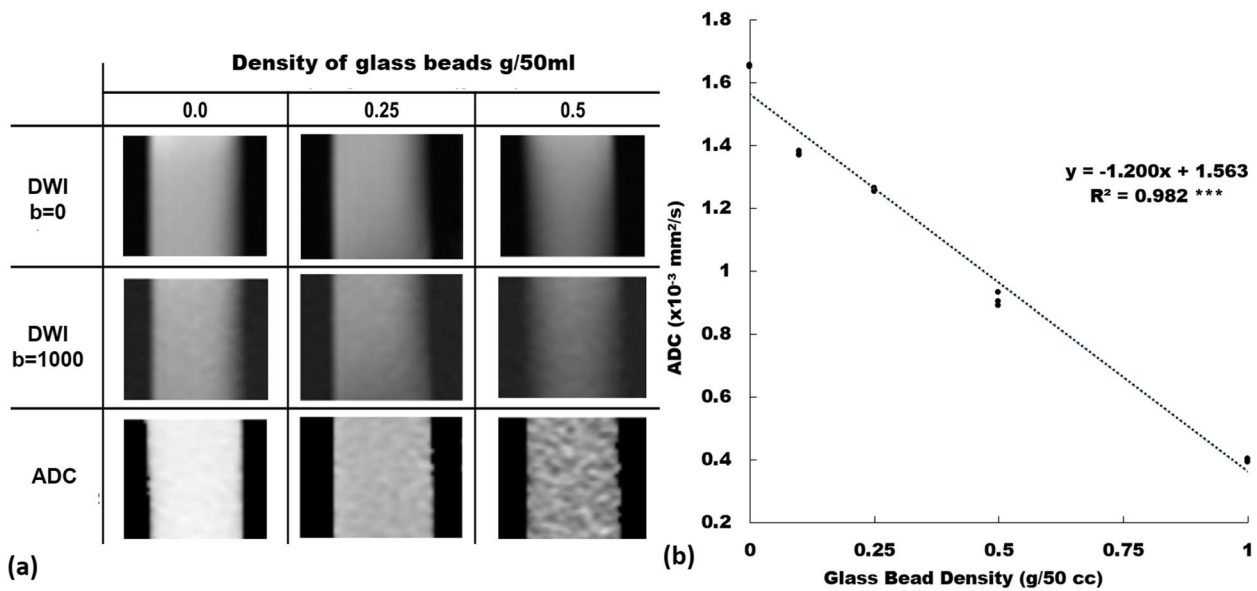


Fig. 6 **a** Diffusion-weighted images ($b = 0$ s/mm² and $b = 1,000$ s/mm²) and ADC maps with a GBD of 0, 0.25, and 0.5 g/mL in water only (0% of fat content, no agarose). **b** Scatter plot and linear regression (dotted line) of ADC versus glass bead density among three independently prepared phantoms. ADC Apparent diffusion coefficient, GBD Glass bead density. *** $p < 0.001$

discrepant impact on the measures of ADC, *i.e.*, a negative association between FC and ADC in some studies [24, 37] but a positive association between FC and ADC in other study [39]. To solve the discrepant clinical observations, a dual-function phantom allowing measures of FC and ADC is demanded. To the best of knowledge, however, a dual-function phantom designed to quantify

the ADC in different FCs and different cellular densities to simulate the real situation of human tissues has not been documented yet.

In this study, we designed the first dual-function phantom, which not only allows us to quantitatively measure the FC and diffusivity of emulsions, respectively, but also enables us to evaluate the relationship among the GBD,

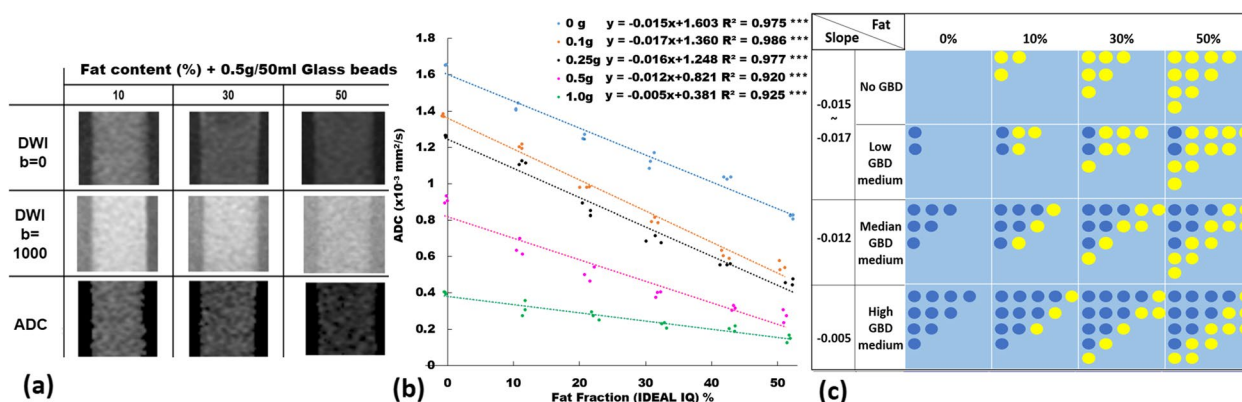


Fig 7 **a** Diffusion-weighted images ($b = 0$ s/mm² and $b = 1,000$ s/mm²) and ADC maps with a GBD 0.5 g/mL with fat content of 10, 30, and 50%. **b** ADC values at different GBD (0, 0.1, 0.25, 0.5, and 1.0 g/50 mL) with respect to different phantom fat fractions measured by IDEAL-IQ (at fat content of 0, 10, 20, 30, 40, and 50%). **c** Each box represents a pixel of the image, containing fat droplets (yellow circles), glass beads (dark blue circles), and water outside the fat droplets and glass beads. ADC Apparent diffusion coefficient, GBD Glass bead density. *** $p < 0.001$

Table 3 ADC of the proposed fat-containing diffusion phantom

GBD g/50 mL	Fat content (%)					
	0	10	20	30	40	50
0	1.653 ± 0.002	1.419 ± 0.020	1.253 ± 0.014	1.124 ± 0.043	1.031 ± 0.006	0.819 ± 0.011
0.1	1.375 ± 0.007	1.205 ± 0.012	0.980 ± 0.002	0.797 ± 0.016	0.608 ± 0.024	0.547 ± 0.027
0.25	1.261 ± 0.005	1.114 ± 0.010	0.855 ± 0.034	0.691 ± 0.020	0.555 ± 0.003	0.458 ± 0.017
0.5	0.909 ± 0.021	0.648 ± 0.045	0.502 ± 0.038	0.393 ± 0.016	0.315 ± 0.014	0.271 ± 0.035
1.0	0.399 ± 0.006	0.312 ± 0.041	0.272 ± 0.023	0.222 ± 0.016	0.202 ± 0.015	0.145 ± 0.021

ADC Apparent diffusion coefficient ($\times 10^{-3}$ mm²/s), FC Fat content (%), GBD Glass bead density (g/50 mL). The ADC value is presented as mean ± standard deviation

FF, and ADC. By adding the agarose into the emulsion, the emulsion becomes a rigid gel at room temperature, thus successfully prolonging the storage period of the phantom on the one hand and preventing oil-water emulsion from dissociation and glass particles from sinking or suspending on the other hand.

The proposed phantom has two different utilities. First, it simulates the fatty environment of human tissues by preparing agarose-based emulsions with six different FCs of 0, 10, 20, 30, 40, and 50%. Second, it imitates water diffusion of human tissues by preparing five different GBDs (0, 0.1, 0.25, 0.5, and 1.0 g/50 mL). Our results showed that the FF is proportional (slope, 1.02~1.05; R^2 , 0.99) to the FC which is similar to that in Bernard’s study [12]. It is worthy to mention that the IDEAL-IQ provides high accuracy of FF in our phantom irrelevant to the GBD (Fig. 3), meaning that we can infuse different GBDs into the fat-water emulsion without altering the FF. In measuring the diffusivity, our results showed that the ADC decreases as the GBD increases similar to that reported in Portakal’s study [11]. The negative association between the ADC and the FF and between the ADC and the

GBD can be attributed to the space for diffusion, which reduces as the FF and the GBD increases.

DWI is a technique that quantifies the water diffusion, reflects the degree of restricted water mobility in biological tissues, and characterizes the relation of the diffusivity with cellularity. Therefore, ADC has been widely used as a biomarker for early diagnosis [40], evaluation of tumor differentiation [41], tumor grade [42], and treatment response [43] of malignancy. Some researchers have reported that the ADC measurement is influenced by the adipose tissue in breast [23], bone [39], and parotid gland [24], attributing to the characteristics of limited diffusion in fatty tissue. However, the potential mixed effect of cellularity and FC on the ADC measurement has not been investigated so far. Our results demonstrated that the effect of the FC and the GBD on the ADC is additive. With a GBD of 0, the ADC is negatively and linearly associated with the FF. Likewise, the ADC is negatively and linearly associated with the GBD with a FF of 0. When glass beads are added, the slope of the linear relationship between the ADC and the FF, however, varies among different GBDs, *i.e.*, the higher the GBD, the lower the slope,

suggesting an additional effect of the GBD. The negative association between ADC and FF in our results is consistent with the findings in Hansmann et al.'s study [44]. Hansmann's study indicated that reduced ADCs by FF varied at different b -values, and our results further reveal that the slope of reduced ADCs with increased FF at $b = 1,000$ is influenced by the initial ADCs with GBD.

It is well known that echo-planar sequences are equipped by fat-suppressed techniques in order to prevent chemical shift ghost artifacts and potential underestimation of ADC [45]. By using fast spin echo "PROPELLER" DWI with fat saturation and without fat saturation, Juan et al. also disclosed that the underestimation of ADC by the non-fat-saturated DWI sequence could be remedied by fat-saturated DWI sequence [46]. Therefore, the influence of fat on the ADC measurement on SS-EP-DWI is usually neglected. Reduced extravascular and extracellular space has been considered to be one of the causes of alternation of tissue perfusion [47]. Results of microscopic examination of our phantom study clearly demonstrate the gradual reduction of space outside the fat droplets and glass beads parallel to the increased amount of fat droplets and glass beads step by step. This observation supports the assumption that the reduced space of diffusion as the main cause of the inverse relationship between ADC and FC and between ADC and GBD. Our results showed reduced diffusion.

Since that both fat droplets and glass beads occupy the space for diffusion of water, it deserves our attention to better characterize the impact of the FF and the GBD on the ADC measurement. First, the ADC is not determined by either the FF or the GBD alone but influenced by the FF and the GBD together. Second, the ADC does not represent the GBD specifically. A GBD with different FFs might have different ADCs. On the other hand, an ADC might be found in different GBDs due to the influence of different FFs. Third, the ADC reflects the GBD with a negative linear association whenever the FF is fixed. Accordingly, to avoid the fat-related bias in the comparison of ADC among different studies and the use of ADC as a biomarker, it is essential to obtain the FF first.

Understanding the relationship among the FF, GBD, and ADC is clinically relevant especially in the fat-rich organs such as breast, liver, and spine as well as in the fat-containing tumors such as lipoma, lipoblastoma, angioliopoma, spindle cell lipoma, pleomorphic lipoma, myolipoma, chondroid lipoma, lipomatosis, hibernoma, fat necrosis, well-differentiated liposarcomas and atypical lipomatous tumors, hepatocellular carcinoma, regenerative nodule, hepatocellular adenoma, focal nodular hyperplasia, and steatosis [48, 49]. By taking the FF into account, clinicians are able to interpret the ADC of a lesion and avoid false positive interpretation as previously encountered [25].

There are some limitations in our study. First, we conducted this study only using the SS-EP-DWI, which has been widely used in daily clinical practice, at a field strength of 1.5 T with a diffusion gradient of $b = 1,000$ s/mm². Hansmann's study [44] evaluated the variation in ADC at different b -values using fat-water phantoms (FF 0%, 20%, 30%, 50%). They found that choice of b -values impacts predicted ADC when fat is present in tissues, and these differences increase with higher FF. In this study, we only employed the mono-exponential DWI model with b -values of 0 and 1,000 s/mm². Factors related to the pulse sequence, b -value, acceleration factor, fat saturated or not, and field strength, which have been shown to influence the measures of ADC [46, 50], were not investigated in the current study. Further studies designed with different pulse sequences, b -value, acceleration factors, fat-saturated conditions, and field strengths to disclose the relationship among the FF, GBD, and ADC are warranted. Nevertheless, we have successfully shown the complex relationship among the FF, GBD, and ADC in this study. Second, the diffusion model was based on the assumption of Gaussian distribution with the ADC calculated based on a mono-exponential equation rather than non-mono-exponential diffusion models, such as kurtosis, stretched exponential, and statistical models. It deserves further studies to evaluate the potential heterogeneity of the proposed phantom. Third, the GBD used in this study is made of hollow glass microspheres with diameters ranging from 20 to 80 μ m, different from human cells by the nature of compositions and size. In order to better simulate the human tissue, we have launched another study using a phantom composed water-filled, lipid bilayers to simulate the human cells to examine the impact of the FC on the ADC measures at different densities of lipid bilayers.

In conclusion, a novel dual-function phantom equipped by different FCs and GBDs was proposed to simulate the human tissue environment and to allow us better quantifying the influence of the FC and GBD on the ADC measures in future clinical practice.

Abbreviations

ADC	Apparent diffusion coefficient
DWI	Diffusion-weighted imaging
FC	Fat content
FF	Fat fraction
GBD	Glass bead density
IDEAL-IQ	Iterative decomposition of water and fat with echo asymmetry and least squares estimation-IQ
MRI	Magnetic resonance imaging
RPM	Revolution per minute
SS-EP-DWI	Single-shot echo-planar diffusion-weighted imaging
SS-EPI	Single-shot echo-planar imaging

Acknowledgements

The authors are grateful for the financial support from China Medical University and Hospital, China Medical University Hsinchu Hospital, and Taiwan Ministry of Science and Technology (Taiwan). Large language models (LLMs): We declare that LLMs such as ChatGPT and Bard etc. were not used in the manuscript.

Authors' contributions

YJL, RHC, HHP, and CJJ formulated the research concept. YJL, YHL, HCC, TYL, CHL, TFL, FYC, and RHC conducted the research design and constructed the study pipeline. JHP and TST conducted the experiments. JHP and YCL contributed to data preparation. HHP, YJL, and CJJ contributed to data cleaning and quality control. YJL wrote the main manuscript. RHC and CJJ substantially edited the manuscript. All authors read and approved the final manuscript.

Funding

•YJL received financial support partly from Taiwan Ministry of Science and Technology (MOST 110-2221-E-035-016).
•JHP received financial support partly from Taiwan Ministry of Science and Technology (MOST 109-2813-C-039-093-B) and China Medical University (CMU109-SR-88).
•CJJ received financial support partly from Taiwan Ministry of Science and Technology (MOST 110-2314-B-039-031).
•FYC and RHC received financial support partly from China Medical University Hospital (DMR-112-173).
•YHL received financial support partly from China Medical University Hsinchu Hospital (CMUHCH-DMR-110-014).

Availability of data and materials

The authors confirm that the data and materials supporting the findings of this study are available on request.

Declarations

Ethics approval and consent to participate

Not applicable. Institutional Review Board approval was not required because this is a phantom-only study.

Consent for publication

Not applicable. The manuscript does not contain data from any individual person.

Competing interests

The authors declare that they have no competing interests.

Author details

¹Department of Automatic Control Engineering, Feng Chia University, Taichung, Taiwan, Republic of China. ²Ph.D. Program in Electrical and Communication Engineering, Feng Chia University, Taichung, Taiwan, Republic of China. ³Department of Medical Imaging, China Medical University Hsinchu Hospital, 199, Sec. 1, Xinglong Rd., Zhubei City, Hsinchu County 302, Taiwan, Republic of China. ⁴Department of Biomedical Engineering and Environmental Sciences, National Tsing Hua University, Hsinchu, Taiwan, Republic of China. ⁵Department of Biomedical Engineering, Chinese University of Hong Kong, Hong Kong, China. ⁶Master's Program of Biomedical Informatics and Biomedical Engineering, Feng Chia University, Taichung, Taiwan, Republic of China. ⁷Cheng Ching Hospital, Taichung, Taiwan, Republic of China. ⁸Institute of Nuclear Engineering and Science, National Tsing Hua University, Hsinchu, Taiwan, Republic of China. ⁹Department of Fiber and Composite Materials, Feng Chia University, Taichung, Taiwan, Republic of China. ¹⁰Department of Medical Imaging, China Medical University Hospital, Taichung, Taiwan, Republic of China. ¹¹Department of Radiology, School of Medicine, China Medical University, Taichung, Taiwan, Republic of China. ¹²Graduate Institute of Biomedical Sciences, China Medical University, Taichung 406, Taiwan, Republic of China. ¹³Center for Molecular Medicine, China Medical University Hospital, Taichung, Taiwan, Republic of China. ¹⁴Department of Medical Laboratory and Biotechnology, Asia University, Taichung, Taiwan, Republic of China.

Received: 18 August 2023 Accepted: 14 November 2023

Published online: 13 February 2024

References

1. Raunig DL, McShane LM, Pennello G et al (2015) Quantitative imaging biomarkers: a review of statistical methods for technical performance assessment. *Stat Methods Med Res* 24:27–67. <https://doi.org/10.1177/0962280214537344>
2. Jack CR Jr, Shiung MM, Gunter JL et al (2004) Comparison of different MRI brain atrophy rate measures with clinical disease progression in AD. *Neurology* 62:591–600. <https://doi.org/10.1212/01.wnl.0000110315.26026.e6>
3. Partridge SC, Gibbs JE, Lu Y et al (2005) MRI measurements of breast tumor volume predict response to neoadjuvant chemotherapy and recurrence-free survival. *AJR Am J Roentgenol* 184:1774–1781. <https://doi.org/10.2214/ajr.184.6.01841774>
4. Wu X, Li R, Fleisher AS et al (2011) Altered default mode network connectivity in Alzheimer's disease—a resting functional MRI and Bayesian network study. *Hum Brain Mapp* 32:1868–1881. <https://doi.org/10.1002/hbm.21153>
5. Reeder SB, Sirlin CB (2010) Quantification of liver fat with magnetic resonance imaging. *Magn Reson Imaging Clin N Am* 18:337–357. <https://doi.org/10.1016/j.mric.2010.08.013>
6. Wu W, Miller KL (2017) Image formation in diffusion MRI: a review of recent technical developments. *J Magn Reson Imaging* 46:646–662. <https://doi.org/10.1002/jmri.25664>
7. Kim HJ, Cho HJ, Kim B et al (2019) Accuracy and precision of proton density fat fraction measurement across field strengths and scan intervals: a phantom and human study. *J Magn Reson Imaging* 50:305–314. <https://doi.org/10.1002/jmri.26575>
8. Keenan KE, Ainslie M, Barker AJ et al (2018) Quantitative magnetic resonance imaging phantoms: a review and the need for a system phantom. *Magn Reson Med* 79:48–61. <https://doi.org/10.1002/mrm.26982>
9. Subhawong TK, Jacobs MA, Fayad LM (2014) Insights into quantitative diffusion-weighted MRI for musculoskeletal tumor imaging. *AJR Am J Roentgenol* 203:560–572. <https://doi.org/10.2214/AJR.13.12165>
10. Sun J, Barnes M, Dowling J, Menk F, Stanwell P, Greer PB (2015) An open source automatic quality assurance (OSAQA) tool for the ACR MRI phantom. *Australas Phys Eng Sci Med* 38:39–46. <https://doi.org/10.1007/s13246-014-0311-8>
11. Portakal ZG, Shermer S, Jenkins C et al (2018) Design and characterization of tissue-mimicking gel phantoms for diffusion kurtosis imaging. *Med Phys* 45:2476–2485. <https://doi.org/10.1002/mp.12907>
12. Bernard CP, Liney GP, Manton DJ, Turnbull LW, Langton CM (2008) Comparison of fat quantification methods: a phantom study at 3.0T. *J Magn Reson Imaging* 27:192–197. <https://doi.org/10.1002/jmri.21201>
13. Hu HH, Yokoo T, Bashir MR et al (2021) Linearity and bias of proton density fat fraction as a quantitative imaging biomarker: a multicenter, multiplatform, multivendor phantom study. *Radiology* 298:640–651. <https://doi.org/10.1148/radiol.2021202912>
14. Keenan KE, Wilmes LJ, Aliu SO et al (2016) Design of a breast phantom for quantitative MRI. *J Magn Reson Imaging* 44:610–619. <https://doi.org/10.1002/jmri.25214>
15. Matsuya R, Kuroda M, Matsumoto Y et al (2009) A new phantom using polyethylene glycol as an apparent diffusion coefficient standard for MR imaging. *Int J Oncol* 35:893–900. https://doi.org/10.3892/ijo_00000404
16. Khasawneh A, Kuroda M, Yoshimura Y et al (2020) Development of a novel phantom using polyethylene glycol for the visualization of restricted diffusion in diffusion kurtosis imaging and apparent diffusion coefficient subtraction method. *Biomed Rep* 13:52. <https://doi.org/10.3892/br.2020.1359>
17. Boursianis T, Kalaitzakis G, Pappas E, Karantanis AH, Maris TG (2021) MRI diffusion phantoms: ADC and relaxometric measurement comparisons between polyacrylamide and agarose gels. *Eur J Radiol* 139:109696. <https://doi.org/10.1016/j.ejrad.2021.109696>
18. Kalaitzakis G, Boursianis T, Gourzoulidis G et al (2020) Apparent diffusion coefficient measurements on a novel diffusion weighted MRI phantom utilizing EPI and HASTE sequences. *Phys Med* 73:179–189. <https://doi.org/10.1016/j.ejmp.2020.04.024>
19. Lavdas I, Behan KC, Papadaki A, McRobbie DW, Aboagye EO (2013) A phantom for diffusion-weighted MRI (DW-MRI). *J Magn Reson Imaging* 38:173–179. <https://doi.org/10.1002/jmri.23950>
20. Hara M, Kuroda M, Ohmura Y et al (2014) A new phantom and empirical formula for apparent diffusion coefficient measurement by a 3 Tesla

- magnetic resonance imaging scanner. *Oncol Lett* 8:819–824. <https://doi.org/10.3892/ol.2014.2187>
21. Delakis I, Moore EM, Leach MO, De Wilde JP (2004) Developing a quality control protocol for diffusion imaging on a clinical MRI system. *Phys Med Biol* 49:1409–1422. <https://doi.org/10.1088/0031-9155/49/8/003>
 22. Mikayama R, Yabuuchi H, Matsumoto R et al (2020) Development of a new phantom simulating extracellular space of tumor cell growth and cell edema for diffusion-weighted magnetic resonance imaging. *MAGMA* 33:507–513. <https://doi.org/10.1007/s10334-019-00823-6>
 23. Partridge SC, Singer L, Sun R et al (2011) Diffusion-weighted MRI: influence of intravoxel fat signal and breast density on breast tumor conspicuity and apparent diffusion coefficient measurements. *Magn Reson Imaging* 29:1215–1221. <https://doi.org/10.1016/j.mri.2011.07.024>
 24. Chang HC, Juan CJ, Chiu HC et al (2014) Effects of gender, age, and body mass index on fat contents and apparent diffusion coefficients in healthy parotid glands: an MRI evaluation. *Eur Radiol* 24:2069–2076. <https://doi.org/10.1007/s00330-014-3265-z>
 25. Pinker K, Moy L, Sutton EJ et al (2018) Diffusion-weighted imaging with apparent diffusion coefficient mapping for breast cancer detection as a stand-alone parameter: comparison with dynamic contrast-enhanced and multiparametric magnetic resonance imaging. *Invest Radiol* 53:587–595. <https://doi.org/10.1097/RLI.0000000000000465>
 26. Merritt S, Gulsen G, Chiou G et al (2003) Comparison of water and lipid content measurements using diffuse optical spectroscopy and MRI in emulsion phantoms. *Technol Cancer Res Treat* 2:563–569. <https://doi.org/10.1177/153303460300200608>
 27. Yu H, McKenzie CA, Shimakawa A et al (2007) Multiecho reconstruction for simultaneous water-fat decomposition and T2* estimation. *J Magn Reson Imaging* 26:1153–1161. <https://doi.org/10.1002/jmri.21090>
 28. Koo TK, Li MY (2016) A guideline of selecting and reporting intraclass correlation coefficients for reliability research. *J Chiropr Med* 15:155–163. <https://doi.org/10.1016/j.jcm.2016.02.012>
 29. Hines CD, Yu H, Shimakawa A, McKenzie CA, Brittain JH, Reeder SB (2009) T1 independent, T2* corrected MRI with accurate spectral modeling for quantification of fat: validation in a fat-water-SPIO phantom. *J Magn Reson Imaging* 30:1215–1222. <https://doi.org/10.1002/jmri.21957>
 30. Hu HH, Nayak KS (2010) Change in the proton T(1) of fat and water in mixture. *Magn Reson Med* 63:494–501. <https://doi.org/10.1002/mrm.22205>
 31. Leporq B, Lambert SA, Ronot M et al (2016) Hepatic fat fraction and visceral adipose tissue fatty acid composition in mice: quantification with 7.0T MRI. *Magn Reson Med* 76:510–518. <https://doi.org/10.1002/mrm.25895>
 32. Navaratna R, Zhao R, Colgan TJ et al (2021) Temperature-corrected proton density fat fraction estimation using chemical shift-encoded MRI in phantoms. *Magn Reson Med* 86:69–81. <https://doi.org/10.1002/mrm.28669>
 33. Starekova J, Hernando D, Pickhardt PJ, Reeder SB (2021) Quantification of liver fat content with CT and MRI: state of the art. *Radiology* 301:250–262. <https://doi.org/10.1148/radiol.2021204288>
 34. Pullens P, Bladt P, Sijbers J, Maas AI, Parizel PM (2017) Technical note: a safe, cheap, and easy-to-use isotropic diffusion MRI phantom for clinical and multicenter studies. *Med Phys* 44:1063–1070. <https://doi.org/10.1002/mp.12101>
 35. Lavdas I, Miquel ME, McRobbie DW, Aboagye EO (2014) Comparison between diffusion-weighted MRI (DW-MRI) at 1.5 and 3 tesla: a phantom study. *J Magn Reson Imaging* 40:682–690. <https://doi.org/10.1002/jmri.24397>
 36. Chang HC, Juan CJ, Chiu HC et al (2013) Parotid fat contents in healthy subjects evaluated with iterative decomposition with echo asymmetry and least squares fat-water separation. *Radiology* 267:918–923. <https://doi.org/10.1148/radiol.12112599>
 37. Colombo A, Bombelli L, Summers PE et al (2021) Effects of sex and age on fat fraction, diffusion-weighted image signal intensity and apparent diffusion coefficient in the bone marrow of asymptomatic individuals: a cross-sectional whole-body MRI study. *Diagnostics* (Basel) 11:913. <https://doi.org/10.3390/diagnostics11050913>
 38. Schmeel FC, Luetkens JA, Wagenhauser PJ et al (2018) Proton density fat fraction (PDFF) MRI for differentiation of benign and malignant vertebral lesions. *Eur Radiol* 28:2397–2405. <https://doi.org/10.1007/s00330-017-5241-x>
 39. Tsujikawa T, Makino A, Oikawa H et al (2022) Assessing the ADC of bone-marrow on whole-body MR images in relation to the fat-suppression method and fat content. *Magn Reson Med Sci* 21:407–413. <https://doi.org/10.2463/mrms.mp.2020-0129>
 40. Hill DK, Kim E, Teruel JR et al (2016) Diffusion-weighted MRI for early detection and characterization of prostate cancer in the transgenic adenocarcinoma of the mouse prostate model. *J Magn Reson Imaging* 43:1207–1217. <https://doi.org/10.1002/jmri.25087>
 41. Sugahara T, Korogi Y, Kochi M et al (1999) Usefulness of diffusion-weighted MRI with echo-planar technique in the evaluation of cellularity in gliomas. *J Magn Reson Imaging* 9:53–60. [https://doi.org/10.1002/\(sici\)1522-2586\(199901\)9:1<53::aid-jmri7>3.0.co;2-2](https://doi.org/10.1002/(sici)1522-2586(199901)9:1<53::aid-jmri7>3.0.co;2-2)
 42. Pui MH, Wang Y (2005) Diffusion and magnetization transfer MRI of brain infarct, infection, and tumor in children. *Clin Imaging* 29:162–171. <https://doi.org/10.1016/j.clinimag.2004.08.001>
 43. Moffat BA, Chenevert TL, Lawrence TS et al (2005) Functional diffusion map: a noninvasive MRI biomarker for early stratification of clinical brain tumor response. *Proc Natl Acad Sci U S A* 102:5524–5529. <https://doi.org/10.1073/pnas.0501532102>
 44. Hansmann J, Hernando D, Reeder SB (2013) Fat confounds the observed apparent diffusion coefficient in patients with hepatic steatosis. *Magn Reson Med* 69:545–552. <https://doi.org/10.1002/mrm.24535>
 45. Lee SH, Shin HJ, Moon WK (2021) Diffusion-weighted magnetic resonance imaging of the breast: standardization of image acquisition and interpretation. *Korean J Radiol* 22:9–22. <https://doi.org/10.3348/kjr.2020.0093>
 46. Juan CJ, Chang HC, Hsueh CJ et al (2009) Salivary glands: echo-planar versus PROPELLER diffusion-weighted MR imaging for assessment of ADCs. *Radiology* 253:144–152. <https://doi.org/10.1148/radiol.2531082228>
 47. Chiu SC, Cheng CC, Chang HC et al (2016) Influence of amplitude-related perfusion parameters in the parotid glands by non-fat-saturated dynamic contrast-enhanced magnetic resonance imaging. *Med Phys* 43:1873. <https://doi.org/10.1118/1.4943798>
 48. Gupta P, Potti TA, Wuertzer SD, Lenchik L, Pacholke DA (2016) Spectrum of fat-containing soft-tissue masses at MR imaging: the common, the uncommon, the characteristic, and the sometimes confusing. *Radiographics* 36:753–766. <https://doi.org/10.1148/rg.2016150133>
 49. Costa AF, Thippavong S, Arnason T, Stueck AE, Clarke SE (2018) Fat-containing liver lesions on imaging: detection and differential diagnosis. *AJR Am J Roentgenol* 210:68–77. <https://doi.org/10.2214/AJR.17.18136>
 50. Thoeny HC, De Keyser F, Boesch C, Hermans R (2004) Diffusion-weighted imaging of the parotid gland: influence of the choice of b-values on the apparent diffusion coefficient value. *J Magn Reson Imaging* 20:786–790. <https://doi.org/10.1002/jmri.20196>

Publisher's Note

Springer Nature remains neutral with regard to jurisdictional claims in published maps and institutional affiliations.